This article has been accepted for publication in IEEE Transactions on Instrumentation and Measurement. This is the author's version which has not been fully edited and content may change prior to final publication. Citation information: DOI 10.1109/TIM.2026.3704228

Error Characterization of Laser Scanner-Based Metrology for Large Reflector Antennas: Effects of Tilt and Measurement Noise

1st Asif Rasha
School of Engineering, Computer and Mathematical Sciences
Auckland University of Technology
Auckland, New Zealand
arasha@aut.ac.nz

2nd Tim Natusch
School of Engineering, Computer and Mathematical Sciences
Auckland University of Technology
Auckland, New Zealand
tim.natusch@aut.ac.nz

3rd Sergei Gulyaev
School of Engineering, Computer and Mathematical Sciences
Auckland University of Technology
Auckland, New Zealand
sergei.gulyaev@aut.ac.nz

***Abstract*—Terrestrial laser scanners (LS) are increasingly applied in large-reflector antenna metrology, but the impact of LS tilt, two-face calibration, and intrinsic random noise has not been quantitatively assessed. This paper presents the first systematic characterization of these error sources for LS-based reflector measurement. A controlled laboratory experiment with nine FARO spheres scanned between 0° and 80° revealed a small linear dependence of baseline residuals on the tilt angle (≈0.005 mm/degree). Two-face measurements confirmed calibration stability under tilt, with differences $\leq$ 0.5 mm (1σ). Monte Carlo propagation of range and angular noise introduced an additional 0.1–0.2 mm (1σ) variability in surface RMS. These contributions were combined into an uncertainty budget according to the guidelines of GUM, resulting in a combined standard uncertainty of 0.65 mm (1σ) and an expanded uncertainty ($k = 2$) of 1.3 mm. These results establish quantitative limits on LS-induced error under significant tilt and demonstrate that LS-based metrology remains robust for large-reflector applications, providing a basis for assessing electromagnetic performance.**

***Index Terms*—Laser Scanner, Large Reflector Antenna, Monte Carlo simulation, Antenna metrology, Antenna efficiency**

I. Introduction

Accurate measurement of reflector surfaces and optical alignment are critical to the performance of large-aperture antennas used in radio astronomy, deep-space communication, and satellite tracking. According to the Ruze criterion [1], antenna gain (G) deteriorates exponentially with increasing surface error (ϵ):

$$G = G_0 e^{-(\frac{4\pi\epsilon}{\lambda})^2} \tag{1}$$

where λ is the observed wavelength. ϵ (in mm) is the root mean square (RMS) of the surface residuals, obtained by fitting the measured reflector surface to its ideal shape. A significant reduction—up to 50% in gain—can occur if ϵ exceeds approximately $\lambda/16$. For an antenna operating at 6 GHz ($\lambda \approx 50$ mm), this corresponds to an RMS of $\approx 3.1\,\mathrm{mm}$. Since reflector efficiency at centimeter and shorter wavelengths is highly sensitive to small geometric deviations and misalignment of antenna surfaces and optics, it is essential to monitor and maintain surface accuracy through high-precision metrology techniques such as laser scanning [2], photogrammetry [3], or radio holography [4].

Radio holography estimates reflector surface deviations by analyzing phase errors in the received electromagnetic field across the antenna aperture. Under favorable signal-to-noise conditions, this method can achieve surface measurements with sub-millimeter-level accuracy [5]. However, its practical implementation requires additional instrumentation such as a reference antenna and stable reference sources, as well as antenna modifications, which can limit its routine use in operational observatories. In comparison, photogrammetry reconstructs three-dimensional geometry from calibrated optical images by triangulating the positions of reflective targets distributed across the reflector surface. While capable of millimeter-level accuracy for large antennas, the method requires extensive marker placement on the antenna surface and is sensitive to environmental factors such as lighting and weather conditions. Although both techniques are well established, their setup complexity can be a constraint when relatively fast and accessible measurements are required.

This limitation is particularly relevant in radio astronomy, where redundant telecommunication antennas are increasingly being converted into radio telescopes for astronomical observations and deep-space communication. Several such conversions have been undertaken or proposed worldwide, including projects in Ghana [6], Greece [7], and New Zealand [8]. Prior to conversion, it is necessary to evaluate the reflector surface quality and determine geometric parameters such as focal length and reflector alignment. Conventional techniques such as holography and photogrammetry require specialized equipment and extensive setup, making them less suitable for relatively quick preliminary assessments. In contrast, terrestrial laser scanning (LS) enables fast acquisition of three-dimensional (3D) measurements with minimal additional instrumentation.

LS directly measures 3D coordinates using LiDAR principles, generating dense point clouds containing millions of spatial samples per scan. Compared to the other techniques, LS requires minimal setup beyond ensuring an adequate field of view (FOV) of the reflector surface. Due to its portability, rapid acquisition, and nominal millimeter-level accuracy, LS has seen increasing adoption in antenna metrology. Early applications demonstrated the feasibility of LS for surface and optics measurements of large radio telescopes such as the Noto and Medicina antennas [9]. Subsequent studies reported LS-based deformation analysis of main reflectors with diameters ranging from 9 m [10] to 32 m [11] using conventional upright LS configurations at a fixed elevation angle from outside the antenna. These studies demonstrated that the LS can capture detailed reflector geometry under ideal mounting conditions. However, they treated the LS as an ideal measurement device and did not explicitly quantify the contribution of instrumental errors to the derived surface accuracy.

Additional investigations have employed LS to quantify gravity-induced elevation-dependent surface deformation and optical misalignment, further demonstrating its practical utility. In such investigations, the LS was retrofitted on the antenna structure and tilted together with the antenna to obtain measurements at different elevation angles. For example, in the 100 m Effelsberg telescope, the LS was mounted upside down on the sub-reflector (SR) structure and operated over different elevation angles to measure the main reflector (MR) surface deformation due to gravity and estimate focal-length variation [12]. More recently, commissioning measurements of a 70 m radio telescope included detailed elevation-dependent geometric characterization to interpret X-band performance variation [13]. While these studies demonstrated the practicality of LS-based measurements in non-upright configurations, the influence of the LS orientation on the accuracy of the measured surfaces was not quantified.

Manufacturers of LS, such as FARO Technologies, recommend upright operation (typically within $\pm 5^{\circ}$) to maintain calibration integrity [14]. In practical antenna retrofits, however, maintaining strict upright orientation may not be feasible due to mounting constraints or field-of-view requirements. While tilting the LS with the antenna can improve surface coverage and reduce occlusion, it may introduce systematic errors in the data. Even under upright operation, LS measurements are affected by intrinsic calibration errors, reflectivity, stochastic range and angular noise, as specified in the Faro Technologies performance documentation [15]. Consequently, elevation-dependent trends observed in reflector measurements may originate either from structural deformation of the antenna or from orientation-dependent behavior of the LS itself, making it necessary to characterize the LS contribution before interpreting such trends.

Elevation-dependent reflector measurements have previously acknowledged potential calibration and LS tilt-related effects. For example, in a 22 m Cassegrain antenna study [16], a Leica LS was retrofitted on a gimbal system attached to the SR structure to maintain upright orientation as the antenna tilted. While this approach mitigated tilt-induced LS effects, the antenna structure caused partial occlusion at low elevation angles, preventing simultaneous scanning of the sub-reflector (SR). In addition to tilt, LS instruments acquire measurements using two internal scanning faces, which can introduce small systematic offsets between observations. To reduce these systematic biases, the study employed two-face measurements combined with bundle adjustment. However, because the LS was deliberately kept upright, the behavior of two-face calibration under substantial LS tilt remained unexplored.

In our earlier work [17], we simultaneously scanned the MR and SR of a 30 m Cassegrain antenna at 10 different elevation angles by retrofitting the LS on the MR surface. Prior to the scan, a preliminary laboratory check for LS tilt was conducted by scanning a certified spherical target (radius 72.5 mm) positioned approximately 1 m from the LS over tilt angles from 0° to 90°. Sphere centers were estimated by least-squares fitting of sampled surface points in FARO SCENE [27]. The resulting 3D point deviations were < 1 mm between 0° to 40° and < 2 mm between 50° to 90°. Although this preliminary test suggested that the instrument could operate under tilt, it was limited to a single target and therefore did not represent telescope-scale measurements involving millions of points. Based on the measurements, we concluded at the time that no elevation-dependent deformation was observable in the MR surface. However, after quantifying the influence of LS tilt in the present study, the MR surface dataset was reexamined. This reanalysis revealed a systematic increase in surface RMS with increasing elevation angle, attributed to the LS tilt rather than structural deformation of the MR surface.

Beyond antenna-specific applications, several studies have investigated calibration and uncertainty characterization of LS. In these studies, LS geometric calibration parameters, e.g., beam offset, mirror tilt, and encoder eccentricity, are estimated by measuring targets from multiple LS positions. Common approaches include the Network [18], Length-consistency, and Two-face calibration methods [19]. A recent review has emphasized that error characterization and mitigation in LS remain active research topics, particularly in separating instrumental, geometric, and environmental error sources in high-accuracy measurements. [20]. In particular, the Length-consistency

TABLE I
COMPARISON OF LS-BASED REFLECTOR METROLOGY STUDIES WITH RESPECT TO LS TILT, TWO-FACE CALIBRATION AND RANDOM MEASUREMENT ERRORS.

References	LS Configuration	Error Types Considered	Key Limitation
[8], [10], [11]	Upright LS	Not explicitly considered	LS treated as ideal instrument
[9], [12], [13]	LS tilted with antenna	Not explicitly considered	LS treated as ideal instrument
[16]	Upright LS	Two-face	Tilt effects mitigated but not quantified
[18] to [22]	General LS analysis	Instrumental, geometric & environmental	Not antenna-specific error characterization
This work	Tilted LS (0°–80°)	Tilt + Two-face + Random	Unified characterization of tilt, two-face and random LS errors

approach uses the fixed distances between stationary targets that remain constant when observed from different LS positions. A similar concept is adopted in this study for LS error characterization and is described in Section II.

Other studies have classified LS error sources into instrumental imperfections, atmospheric effects, geometric distortions related to LS setup and incidence angle, and object-dependent effects associated with surface reflectivity and material properties [21] [22]. Atmospheric and object-dependent effects are generally minimal in reflector metrology, since antenna surfaces are typically highly reflective aluminum structures and measurements are conducted under stable and favorable weather conditions. While these classifications provide a useful framework for understanding LS accuracy, they do not specifically examine how LS orientation (tilt) influences surface RMS measurements of large reflectors.

Broadly, three categories of LS error are relevant to reflector metrology:

- **Tilt-induced error** — systematic distortion introduced when the LS operates outside its recommended upright orientation.
- **Two-face calibration error** — potential systematic offsets between measurements acquired in the LS two internal scanning faces, which may further vary with tilt.
- **Random error** — stochastic fluctuations in range and angular measurements specified in manufacturer performance specifications.

Despite the increasing use of LS in antenna metrology, a quantitative framework that characterizes tilt-induced distortion, two-face calibration stability, and random measurement noise, and evaluates their combined impact on reflector surface RMS, remains lacking. The goal of this paper is to:

1) Quantify tilt-induced geometric distortions in a FARO LS.
2) Assess the stability of two-face calibration under significant tilt conditions.
3) Propagate manufacturer-specified range and angular noise through a complete reflector-metrology workflow using Monte Carlo simulation [23].
4) Develop a unified, GUM-compliant [24] uncertainty budget integrating tilt bias, two-face calibration effects, and random noise.

Together, these results provide a comprehensive characterization of uncertainty in LS-based reflector metrology and quantify the extent to which LS-induced effects influence measured antenna surface accuracy.

Preliminary results, including Fig. 2 and 3, were presented at the IEEE CAMA 2024 conference [25], where tilt and random noise effects were reported without a complete uncertainty budget. The present manuscript substantially extends that work by incorporating a two-face-under-tilt analysis, developing a unified error budget, and interpreting the resulting uncertainty in the context of antenna gain and surface accuracy measurements.

II. MATERIALS AND METHODS

A. Laser Scanner Specification

All measurements were performed using a FARO Focus S70 terrestrial laser scanner. According to the manufacturer's performance specifications [15], the instrument provides a nominal 3D point accuracy of $\pm$ 2 mm at 10 m, with range noise of approximately $\pm$ 1 mm (1σ) and angular accuracy of approximately $\pm$ 19 arcseconds (1σ) in both horizontal and vertical directions. The instrument is specified for operation within an ambient temperature range of approximately -20° to 55°C.

The LS acquires a full 4π steradian through a $180°$ azimuth rotation and internally performs self-calibration between its two scanning faces. Manufacturer guidelines recommend upright operation within approximately $\pm$ $5°$ to preserve calibration integrity [14].

In addition, nine spherical targets (radius 72.5 mm) were used to evaluate LS tilt and two-face errors. These FARO-manufactured laser scanning targets have a diffuse, high-contrast surface, enabling reliable automatic detection and center estimation in FARO SCENE software [26].

B. Experimental Setup and Rationale

Evaluating the impact of LS tilt on surface measurement accuracy requires isolating the intrinsic LS error from scene-dependent measurement errors. To achieve this, a controlled laboratory experiment was conducted. A large lecture theater $(20 \times 12$ m$)$ was selected to approximate

This article has been accepted for publication in IEEE Transactions on Instrumentation and Measurement. This is the author's version which has not been fully edited and content may change prior to final publication. Citation information: DOI 10.1109/TIM.2026.3704228

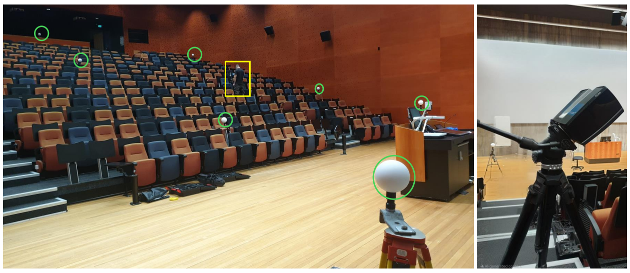

Fig. 1. Left: Distribution of spherical targets (green) in the theatre relative to the scanner position (yellow). Right: The pan-and-tilt mount and tilted scanner used in this work. This configuration enables controlled evaluation of tilt-induced geometric effects.

the size of a 30 m parabolic dish, and the spherical targets were distributed at varying heights and distances. The FARO Focus LS was mounted on a pan-and-tilt tripod and incrementally tilted from 0° to 80° in 10° steps, as shown in Fig. 1. This configuration enables consistent geometric comparisons across tilt angles while eliminating any variability introduced by the scanned object. The spatial layout of the nine targets and the corresponding baselines are shown in Fig. 2.

All scans were registered relative to the 0° reference using FARO SCENE software [27], which automatically detected spherical targets and estimated their centers for scan registration. Each spherical target is represented by a dense set of points, typically ranging from hundreds to thousands depending on its distance from the LS. The center of each sphere is estimated using least-squares fitting [28]. A search radius of $r = \pm 0.0725$ m was applied as a detection criterion in FARO Scene. Occasional false detections occurred when non-spherical objects in the scans matched the radius tolerance. These were removed through manual inspection.

Measurements were conducted under controlled static indoor conditions (approximately 20–22°C), well within the manufacturer's specified operating range. For each tilt configuration, nine reference spheres were scanned and their centers estimated from the acquired point cloud. The distances between all sphere pairs were then computed, resulting in $\binom{9}{2} = 36$ inter-sphere baselines per scan. Across the eight tilt angles considered in this study, this produced a total of 36 × 8 = 288 baseline residuals used for the statistical analysis. These residuals provided multiple distance measurements among the targets, allowing the tilt effect to be evaluated. The residuals at each tilt angle are derived from a single scan and are therefore not fully independent. However, the available baseline combinations still provide a consistent indication of the trend of tilt-induced bias across the network, as shown in Fig. 5. Future work could include repeated scans at each tilt angle to further quantify measurement repeatability.

Additionally, two-face measurements were conducted at 0°, 50°, and 80° to assess face-to-face calibration

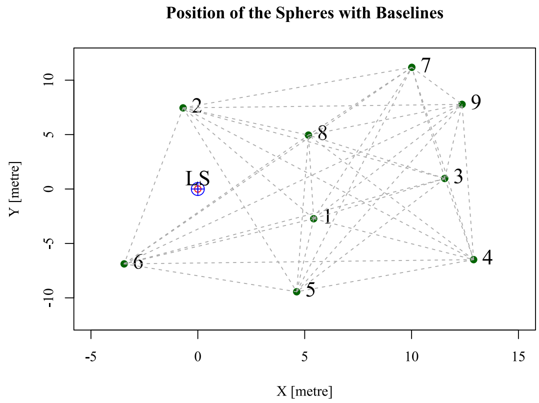

Fig. 2. Top-down layout of the nine spherical targets. The spatial distribution and 36 inter-sphere baselines are shown, providing scale and geometric context for the tilt experiment. This figure is reproduced from our IEEE CAMA 2024 conference paper [25].

differences of the LS at those angles.

C. *Baseline Computation and Residual Definition*

The Euclidean distance (baseline) between every pair of the nine registered sphere centers was computed for each LS tilt angle θ, yielding $\binom{9}{2} = 36$ baseline values per scan. Let $\mathbf{c}_n(\theta) = [p_n(\theta), q_n(\theta), r_n(\theta)]$ denote the center of sphere n in the LS coordinate system after registration relative to the 0° reference. The baseline length B_{nm} (in meters) for the pair (n, m) is

$$\begin{aligned} B_{nm}(\theta) &= \left\|\mathbf{c}_n(\theta) - \mathbf{c}_m(\theta)\right\|_2 \\ &= \sqrt{(p_n - p_m)^2 + (q_n - q_m)^2 + (r_n - r_m)^2}. \end{aligned} \tag{2}$$

The tilt-induced baseline residuals were defined relative to the 0° scan:

$$\Delta B_{nm}(\theta_i) = B_{nm}(0^\circ) - B_{nm}(\theta_i). \tag{3}$$

Here $\theta_i \in \{10^\circ, 20^\circ, \ldots, 80^\circ\}$.

A positive ΔB_{nm} indicates a shorter baseline at tilt θ_i compared to tilt at 0°.

D. *Two-Face Measurement Procedure*

In [16], the author used Leica LS to analyze elevation-dependent deformation of the Onsala 20-m radio telescope. The Leica LS acquires a full 4π steradian scan by rotating through 180° in azimuth using two internal scanning faces (front and back), which can introduce small calibration offsets between the two measurement faces. A *two-face* measurement is performed by scanning the same scene twice: face 1 from 0° to 180°, and face 2 from 180° to 360°. The two datasets, which overlap in coverage, were subsequently combined using a bundle adjustment method to identify and correct systematic biases.

This article has been accepted for publication in IEEE Transactions on Instrumentation and Measurement. This is the author's version which has not been fully edited and content may change prior to final publication. Citation information: DOI 10.1109/TIM.2026.3704228

TABLE II

STATISTICS OF INDIVIDUAL BASELINES: MEAN (μ) AND STANDARD DEVIATION (σ) [MM] OF RESIDUALS OVER TILT ANGLES.

Baseline	1	2	3	4	5	6	7	8
2	-0.04, 0.21							
3	-1.61, 0.51	0.61, 0.36						
4	-0.17, 0.13	-0.09, 0.20	-1.70, 0.35					
5	1.09, 0.38	0.35, 0.35	-0.94, 0.39	0.44, 0.28				
6	1.06, 0.40	0.49, 0.23	-0.49, 0.15	0.29, 0.20	0.04, 0.10			
7	-0.98, 0.33	0.49, 0.14	0.54, 0.49	-1.21, 0.41	-0.28, 0.38	0.23, 0.16		
8	-1.09, 0.33	0.28, 0.18	0.35, 0.67	-0.66, 0.67	-0.12, 0.56	0.05, 0.39	0.28, 0.14	
9	-1.92, 0.51	0.82, 0.18	-0.40, 0.41	-2.32, 0.30	-1.10, 0.40	-0.33, 0.12	1.04, 0.35	0.23, 0.13

FARO LS also covers 4π steradians with a 180° rotation. However, after each scan, the instrument executes a brief internal reorientation as part of its self-calibration. This process introduces substantial overlap between face 1 and face 2 point clouds, which helps to stabilize the internal self-calibration.

To assess whether this calibration remains reliable under LS tilt, we performed two-face scans at 0°, 50°, and 80°. For each tilt, the 36 inter-sphere baselines were processed separately for face 1 and face 2 using the same technique for the tilt test, and the residual differences (face 1 - face 2) were computed.

E. Random Error Propagation Using Monte Carlo Simulation

As outlined in Section I, the Faro LS exhibits three primary random error sources: range noise (approximately ± 1 mm, 1σ), horizontal and vertical angular errors (about $19''$, 1σ each). To quantify how these errors propagate through reflector metrology, we applied a Monte Carlo simulation [23] to the full-dish scans previously acquired in our previous study [17]. That dataset included main reflector (MR) measurements at zenith angles ranging from 0° to 80° in 10° steps, plus an additional scan at 84°.

For each original scan, 100 synthetic point clouds were generated by injecting independent random errors drawn from a normal distribution according to the manufacturer specifications: $N(0, 1\text{ mm})$ for range and $N(0, 19'')$ for both horizontal and vertical angles. Each realization was subsequently processed according to the workflow used in [17]:

1) Coordinate transformation of the MR and SR from the reference frame of the LS to a global origin of a rotational paraboloid (MR) centered at the origin.
2) This was done by using Principal Component Analysis (PCA) for rotation and least-squares for translation.
3) Fitting modeled surfaces to estimate the surface RMS residuals.

The standard deviation of RMS values across all realizations (100 Monte Carlo simulations plus the original dataset) was taken as the uncertainty due to random LS noise.

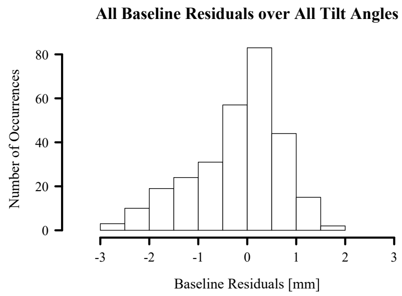

Fig. 3. Histogram of baseline residuals $\Delta B_{nm}(\theta_i)$ aggregated over all baselines and tilt angles (10°–80°). The distribution shows slight skew with some outliers, mainly associated with baselines involving a partially occluded sphere. This figure is reproduced from our IEEE CAMA 2024 conference paper [25].

III. RESULTS

A. Tilt-Induced Baseline Residuals

Across all baselines and tilt angles (36 baselines $\times$ 8 angles = 288 residuals), the distribution shows a mean of -0.19 mm and a standard deviation of 0.90 mm. Figure 3 shows a histogram of all residuals; the distribution is slightly skewed with a few outliers. Inspection of point counts revealed that one sphere (no. 9 in Fig. 2) was partially occluded, yielding fewer points and higher center-fit uncertainty. Excluding baselines involving sphere 9 produces slightly improved statistics: mean -0.10 mm and standard deviation 0.80 mm. Although the histogram is slightly skewed, the distribution remains approximately unimodal and centered near zero. Therefore, the standard deviation is used as a measure of dispersion for the residuals.

Table II reports the per-baseline mean (μ) and standard deviation (σ) of $\Delta B_{nm}(\theta_i)$ across the eight tilt angles. Baselines involving sphere 9 exhibit larger $|\mu|$ (notably 9–1 and 9–4, with magnitudes near 2 mm), which is consistent with its partial occlusion.

B. Two-Face Calibration Stability

Table III summarizes the resulting mean (μ), standard deviation (σ), and 95% confidence intervals (CIs) of the baseline differences.

The mean baseline differences at all tilt angles are statistically indistinguishable from zero (two-sided one-sample

This article has been accepted for publication in IEEE Transactions on Instrumentation and Measurement. This is the author's version which has not been fully edited and content may change prior to final publication. Citation information: DOI 10.1109/TIM.2026.3704228

TABLE III
TWO-FACE BASELINE DIFFERENCES AT THREE TILT ANGLES, SHOWING CALIBRATION STABILITY UNDER TILT.EACH STATISTIC IS COMPUTED FROM N = 36 INTER-SPHERE BASELINES FOR THE CORRESPONDING TILT ANGLE.

Tilt (°)	N	μ (mm)	σ (mm)	95% CI for μ (mm)
0	36	-0.10	0.50	[-0.27, +0.07]
50	36	+0.04	0.40	[-0.10, +0.18]
80	36	-0.02	0.40	[-0.16, +0.12]

t-tests, $p > 0.2$). The standard deviation remained below 0.5 mm, and the 95% confidence intervals for the means were narrow (within $\pm$0.2 mm). Although the FARO LS has a nominal 3D point accuracy of $\pm$ 2 mm at 10 m, this specification applies to individual measured points. In this study, each spherical target is represented by hundreds of points used to estimate the sphere center. Consequently, the uncertainty of the fitted sphere centers, and therefore the baseline distances, is significantly smaller than the uncertainty of a single point measurement.

This approach extends prior Leica-based upright two-face studies [16] by demonstrating that FARO LS maintains calibration stability even when tilted well beyond the manufacturer's recommended $\pm 5°$ range. For antenna metrology, where upright mounting is often impractical, this result provides evidence that tilted two-face operation does not degrade measurement fidelity.

C. Random Error Propagation Results

Results from the Monte Carlo Simulation showed that the additional variability in RMS residuals is consistently small, typically ranging between 0.1 to 0.2 mm for both MR and SR. These values fall well below the scanner's nominal 3D point accuracy (±2 mm at 10 m), indicating that random LS noise has a negligible effect on reflector measurement accuracy.

This Monte Carlo procedure corresponds directly to the Monte Carlo method of uncertainty propagation described in the Guide to the Expression of Uncertainty in Measurement (GUM). In Section IV, we compare these results against the GUM linearized approach.

IV. ERROR BUDGET AND DISCUSSION

A. Unified Uncertainty Budget

Figures 4 and 5 illustrate the random and systematic LS-induced errors. Fig. 4 shows the RMS of the MR surface residuals from the 2019 surface measurements [17] versus zenith angle, including Monte Carlo–derived error bars. A weak but statistically significant slope of approximately 0.0056 mm per degree was observed (95% CI: 0.003 to 0.009 mm/degree), indicating tilt-related linear correlation across zenith angle.

Fig. 5 complements this result by isolating the same effect under controlled laboratory conditions as discussed in sections II and III. The mean baseline residuals exhibit an almost identical slope (0.005 mm per degree), confirming

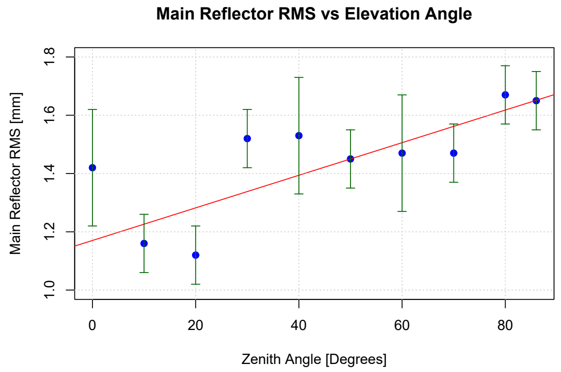

Fig. 4. Main-reflector RMS versus zenith angle from our 2019 study [17], with Monte Carlo–derived uncertainty bars ($\pm 1\sigma$). The variability is consistently 0.1 to 0.2 mm. A weak but statistically significant slope (0.0056 mm/degree) indicates a tilt-related linear correlation (95% CI: 0.003 to 0.009 mm/degree, adjusted $R^2 = 0.63$).

that the observed linear correlation originates from LS tilt geometry rather than structural deformation of the antenna. Because the two analyses are independent and were performed using the same LS, their close agreement strengthens confidence that the observed effect is attributable to LS tilt. Figure 4 is derived from MR data, whereas Fig. 5 is based on laboratory baseline measurements. A slope of 0.005 mm per degree, propagated over the full elevation range of $84°$, results in a tilt-induced uncertainty of 0.005 $\times$ 84 = 0.42 mm. This tilt-induced uncertainty (u_{tilt}) is accounted for when estimating the combined uncertainty using the GUM framework in Eq. (4).

The two-face (u_{face}) contribution was obtained from the baseline statistics of the face-to-face measurements performed at tilt angles of $0°$, $50°$, and $80°$. The RMS dispersion of the baseline residuals ranged between approximately 0.4 and 0.5 mm, and a representative value of U_{face} = 0.45 mm was adopted.

The random noise contribution u_{rand} was derived from Monte-Carlo simulations that propagated the manufacturer-specified range and angular uncertainties of the LS through the RMS of the reflector surface measurement workflow. Across all realizations and tilt angles, the standard deviation of the surface RMS ranged from 0.1 to 0.2 mm for both the main reflector (MR) and the sub-reflector (SR). A conservative representative value of U_{rand} = 0.2 mm was therefore adopted.

These results provide quantitative estimates of both random and systematic LS contributions. They form the basis for constructing a unified uncertainty budget for reflector surface measurements, in accordance with the GUM framework.

Table IV summarizes the uncertainty budget according to GUM. The GUM distinguishes between **Type A** uncertainties, evaluated from statistical analysis of repeated observations, and **Type B** uncertainties, evaluated from

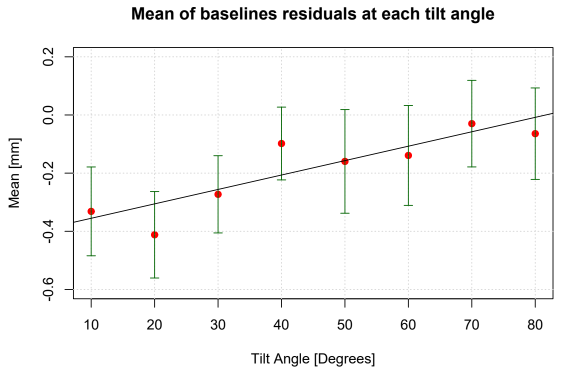

Fig. 5. Mean baseline residual versus LS tilt angle (error bars show standard error across 36 baselines). The linear correlation (resulting in a slope of 0.005 mm/degree, 95% CI: 0.002–0.008 mm/degree, adjusted $R^2 = 0.71$) matches the result in Fig. 4, confirming that the elevation-dependent slope originates from LS tilt.

other sources such as instrument specifications, calibration data, or analytical models. In this study, all three contributions are treated as Type B uncertainties, arising from instrument characteristics or modeled effects rather than repeated measurements of the quantity itself.

It should be noted that the baseline residuals used to estimate tilt and two-face errors (0.42 mm and 0.45 mm, respectively) are derived directly from the measured point clouds and therefore inherently include the effects of LS range and angular errors. In contrast, the Monte Carlo analysis propagates these errors separately through the surface RMS calculation workflow, quantifying their contribution to the surface RMS uncertainty.

Following the GUM framework, the combined standard uncertainty u_c is obtained by propagating independent sources in quadrature:

$$u_c = \sqrt{u_{\text{tilt}}^2 + u_{\text{face}}^2 + u_{\text{rand}}^2} \tag{4}$$

where u_{tilt}, u_{face}, and u_{rand} are the standard uncertainties due to tilt bias, two-face calibration, and random noise propagation, respectively.

Adopting representative values from Table IV, ($u_{\text{tilt}} = 0.42$ mm, $u_{\text{face}} = 0.45$ mm, $u_{\text{rand}} = 0.20$ mm), the combined standard uncertainty becomes:

$$u_c = \sqrt{(0.42)^2 + (0.45)^2 + (0.20)^2} \approx 0.65 \text{ mm}.$$

The expanded uncertainty, U, for coverage factor k=2, is therefore

$$U = k\, u_c \approx 1.3 \text{ mm}$$

corresponding to ≈ 95 % confidence interval. The combined uncertainty budget derived allows the contribution of LS measurement uncertainty to be interpreted for the earlier reflector measurements. The reported surface RMS of 1.1–1.7 mm across 10 elevation angles in the 2019 study [17] includes contributions from both the true structural surface deviation and the LS measurement uncertainty. The observed RMS of the surface can be represented as the quadrature sum of the instrument uncertainty and structural surface error. The effective RMS σ_{eff} (in mm) can therefore be written as [10]:

$$\sigma_{\text{eff}} = \sqrt{\sigma_{\text{struct}}^2 + u_c^2}. \tag{5}$$

where σ_{struct} represents the structural surface RMS (in mm) and u_c is the combined uncertainty of the LS (0.65 mm) determined in this work. For a representative surface roughness of 1.5 mm, the effective RMS, including measurement uncertainty, is approximately 1.64 mm. The intrinsic LS contribution is therefore quantifiable but small relative to the structural surface variation.

B. Impact on Antenna Gain

For an antenna operating at 6 GHz, a deviation of $\sigma_{\text{struct}} = 1.5$ mm translates into 15% loss in antenna gain according the Ruze equation (Eq. 1). When the LS uncertainty of $u_c = 0.65$ mm is included, the effective RMS σ_{eff} increases to 1.64 mm, which translates into a loss of 18.3%. Thus, LS-induced uncertainty contributes very little to the dispersion in gain-loss predictions, while the mean performance remains dominated by the reflector's structural surface accuracy.

V. Conclusion

This study quantified the effects of LS tilt, two-face calibration bias, and random measurement noise on the surface RMS measurement of large reflector antennas. A controlled tilt experiment with nine spherical targets established a small, linear dependence of baseline residuals on tilt angle ($\approx$ 0.005 mm per degree), confirming that tilt-induced geometric effects are minimal compared to the LS nominal $\pm$ 2 mm 3D point accuracy. Two-face calibration integrity remained stable, showing differences $\leq$0.5 mm, and Monte Carlo simulations showed that random noise contributed with a dispersion of only 0.1 to 0.2 mm of variability to surface RMS across elevations. Significantly, the same tilt-related slope was independently verified in a reanalysis of the 30 m antenna measurements [17], in which the LS was tilted in situ, confirming that this trend arises from LS tilt rather than from reflector deformation. Overall, LS-induced effects are small relative to typical reflector surface variations, confirming the suitability of LS-based metrology even under non-ideal mounting conditions.

In constructing the unified uncertainty model, tilt, random, and two-face contributions were treated as independent and were combined in quadrature. Although some interaction between these error sources cannot be ruled out—for instance, tilt may slightly influence two-face calibration—their physical origins are distinct, so

TABLE IV
ERROR BUDGET FOR LS-BASED REFLECTOR MEASUREMENTS

Error Source	Error (mm)	Evaluation Method
Tilt-induced bias	0.42	Regression slope (0.005 mm/deg) propagated over maximum antenna tilt (84° zenith angle)
Two-face calibration differences	0.45	RMS dispersion of baseline residuals between scanner faces at 0°, 50°, and 80° tilt
Random measurement noise (MR/SR)	0.20	Standard deviation of surface RMS from Monte Carlo propagation of range and angular errors

treating them as independent provides a good practical approximation. Moreover, each term contributes only to a small amount of the total uncertainty budget, thus yielding a combined standard uncertainty of ≈ 0.65 mm (1σ). This work therefore provides a systematic uncertainty characterization framework for LS-based reflector metrology, clarifying how LS-induced effects influence measured surface RMS and antenna gain estimation. The results demonstrate that even under significant LS tilt, the resulting measurement uncertainty remains well below typical reflector surface tolerances required for centimeter-wavelength radio astronomy.

Beyond the methodological contribution, the proposed framework offers a practical methodology for interpreting LS-derived reflector measurements and distinguishing LS-induced trends from true structural deformation. This is particularly relevant for rapid geometric assessment of large antennas, including redundant telecommunications antennas under consideration for conversion into radio telescopes for radio astronomy and deep-space communication.

Future work should extend this analysis to other LS models and measurement configurations to compare orientation-dependent behavior across instruments. Applying the proposed uncertainty framework to very large antennas (diameter ≥ 50 m), where measurement range and geometric effects become more significant.In addition, incorporating machine-learning-based uncertainty modeling [29] offers a promising approach for improving the accuracy and reliability of future LS-based antenna measurements.

REFERENCES

[1] W. White and L. Desize, "Focal length of a Cassegrain reflector," *IRE Trans. Antennas Propag.*, vol. 9, no. 4, p. 412, 1961, doi: 10.1109/TAP.1961.1145010.

[2] C. Holst, A. Nothnagel, R. Haas, and H. Kuhlmann, "Investigating the gravitational stability of a radio telescope's reference point using a terrestrial laser scanner: Case study at the Onsala Space Observatory 20-m radio telescope," *ISPRS J. Photogramm. Remote Sens.*, vol. 149, pp. 67–76, 2019.

[3] M. Lösler, C. Eschelbach, A. Greiwe, B. Zhou, and L. McCallum, "Innovative approach for modelling gravity-induced signal path variations of VLBI radio telescopes," *Earth Planets Space*, vol. 77, no. 1, Art. no. 9, 2025.

[4] G. Serra, P. Bolli, G. Busonera, T. Pisanu, S. Poppi, F. Gaudiomonte, G. Zacchiroli, J. Roda, M. Morsiani, and J. A. Lopez-Perez, "The microwave holography system for the Sardinia radio telescope," in *Ground-based and Airborne Telescopes IV*, vol. 8444, SPIE Proc., 2012, pp. 1877–1891.

[5] A. V. Räisänen, J. Ala-Laurinaho, T. Crowe, S. Pivnenko, M. S. Castañer, and V. Viikari, "Antenna measurements at millimeter and submillimeter wavelengths," in *Aperture Antennas for Millimeter and Sub-Millimeter Wave Applications*, A. Boriskin and R. Sauleau, Eds. Cham, Switzerland: Springer, 2018, pp. 409–450.

[6] E. Proven-Adzri, N. Imara, T. Ansah-Narh, W. Sewavi, D. Klutse, E. Iyida, J. B. Tandoh, N. A. Frimpong, B. Woode, and P. Pretorius, "Ghana radio astronomy observatory," *J. Astron. Telesc. Instrum. Syst.*, vol. 12, no. 1, p. 017001, 2026.

[7] N. Gizani and G. P. Veldes, "On Greece's participation to the radio detection of extraterrestrial technosignatures," in *Proc. COSPAR Scientific Assembly*, vol. 44, 2022, p. 2820.

[8] L. Woodburn, T. Natusch, S. Weston, P. Thomasson, M. Godwin, C. Granet, and S. Gulyaev, "Conversion of a New Zealand 30-metre telecommunications antenna into a radio telescope," *Publ. Astron. Soc. Aust.*, vol. 32, Art. no. e017, 2015.

[9] P. Sarti, L. Vittuari, and C. Abbondanza, "Laser scanner and terrestrial surveying applied to gravitational deformation monitoring of large VLBI telescopes' primary reflector," *J. Surv. Eng.*, vol. 135, no. 4, pp. 136–148, Nov. 2009.

[10] D. Belton, A. Gibson, B. Stansby, S. Tingay, and K.-H. Bae, "Modelling of an inexpensive 9 m satellite dish from 3D point clouds captured by terrestrial laser scanners," *Int. Arch. Photogramm., Remote Sens. Spatial Inf. Sci.*, vol. 38, pp. 313–318, 2012.

[11] M. Bleiders, "Electromagnetic model of dual reflector radio telescope based on laser scanning survey," in *Proc. IEEE MTTW*, 2020, vol. 1, pp. 217–221.

[12] C. Holst, P. Zeimetz, A. Nothnagel, W. Schauerte, and H. Kuhlmann, "Estimation of focal length variations of a 100-m radio telescope's main reflector by laser scanner measurements," *J. Surv. Eng.*, vol. 138, no. 3, pp. 126–135, Aug. 2012.

[13] L.-B. Fu, J.-J. Liu, W. Yan, D.-Q. Kong, X. Ren, C.-D. Liu, and H.-B. Zhang, "Gravitational deformation measurement method for the main reflector and sub-reflector of the 70 m antenna by laser scanner," *Res. Astron. Astrophys.*, vol. 22, no. 9, Art. no. 095001, 2022.

[14] FARO Technologies, "Laser scanner best practices," 2023. [Online]. Available: https://knowledge.faro.com/. [Accessed: Dec. 2023].

[15] FARO Technologies, "Performance specification," 2023. [Online]. Available: https://media.faro.com/. [Accessed: Dec. 2023].

[16] C. Holst, D. Schunck, A. Nothnagel, R. Haas, L. Wennerbäck, H. Olofsson, R. Hammargren, and H. Kuhlmann, "Terrestrial laser scanner two-face measurements for analyzing the elevation-dependent deformation of the Onsala space observatory 20-m radio telescope's main reflector in a bundle adjustment," *Sensors*, vol. 17, no. 8, p. 1833, 2017.

[17] A. R. Rasha, T. Natusch, C. Granet, and S. Gulyaev, "Conversion of a telecommunications antenna into a radio telescope: Laser scanner measurements of optics and dish surface quality of a Cassegrain antenna," *J. Astron. Instrum.*, vol. 8, no. 3, p. 1950010, 2019.

[18] S. Shi, B. Muralikrishnan, and D. Sawyer, "Terrestrial laser scanner calibration and performance evaluation using the network method," *Opt. Lasers Eng.*, vol. 134, p. 106298, 2020.

[19] B. Muralikrishnan, L. Wang, P. Rachakonda, and D. Sawyer, "Terrestrial laser scanner geometric error model parameter correlations in the Two-face, Length-consistency, and Network methods of self-calibration," *Precision Engineering*, vol. 52, pp. 15–29, 2018.

[20] M. Sabzali and L. Pilgrim, "A comprehensive review of mathematical error characterization and mitigation strategies in terrestrial laser scanning," Remote Sens., vol. 17, no. 14, p. 2528, 2025.

[21] V. Hlotov and Kh. Marusazh, "Accuracy investigation of point clouds with FARO Focus 3D S120 terrestrial laser scanner," *Geodesy, Cartography and Aerial Photography*, vol. 90, pp. 41–49, 2019.
[22] M. Barbarella, M. Fiani, and A. Lugli, "Uncertainty in terrestrial laser scanner surveys of landslides," *Remote Sensing*, vol. 9, no. 2, p. 113, 2017.
[23] R. L. Harrison, "Introduction to Monte Carlo simulation," in *AIP Conf. Proc.*, vol. 1204, 2010, pp. 17–21, doi: 10.1063/1.3295638.
[24] JCGM, "Evaluation of measurement data—Guide to the expression of uncertainty in measurement," JCGM 100:2008, Joint Committee for Guides in Metrology, 2008.
[25] A. Rasha, T. Natusch, and S. Gulyaev, "Effect of terrestrial laser scanner tilt on radio telescope surface measurement accuracy," in *Proc. IEEE Conf. Antenna Meas. Appl. (CAMA)*, 2024, pp. 1–3, doi: 10.1109/CAMA62287.2024.10986100.
[26] FARO Technologies Inc., *Traceable 3D Accessories Guide*, Mar. 2026. [Online]. Available: https://knowledge.faro.com/
[27] FARO Technologies, Inc., *FARO SCENE User Manual*, 2024. [Online]. Available: https://www.faro.com/.
[28] Y. Shi, G. Zhao, M. Wang, Y. Xu, and D. Zhu, "An algorithm for fitting sphere target of terrestrial LiDAR," *Sensors*, vol. 21, no. 22, p. 7546, 2021.
[29] J. Hartmann and H. Alkhatib, "Uncertainty modelling of laser scanning point clouds using machine-learning methods," *Remote Sens.*, vol. 15, no. 9, Art. no. 2349, 2023, doi: 10.3390/rs15092349.